

Data report: raw and normalized elemental data along the Site U1338 splice from X-ray fluorescence scanning¹

Mitchell Lyle,² Annette Olivarez Lyle, Thomas Gorgas,³ Ann Holbourn,⁴ Thomas Westerhold,⁵ Ed Hathorne,⁶ Katsunori Kimoto,⁷ and Shinya Yamamoto⁸

Chapter contents

Abstract	1
Introduction	1
X-ray fluorescence analytical technique	2
Data acquisition methods	2
Data reduction methods for later calibration: normalized median-scaled method	3
Example calibration of data: BaSO₄	5
Results and discussion	5
Conclusions	6
Acknowledgments	6
References	6
Figures	8
Tables	16

¹Lyle, M., Olivarez Lyle, A., Gorgas, T., Holbourn, A., Westerhold, T., Hathorne, E., Kimoto, K., and Yamamoto, S., 2012. Data report: raw and normalized elemental data along the Site U1338 splice from X-ray fluorescence scanning. *In* Pälike, H., Lyle, M., Nishi, H., Raffi, I., Gamage, K., Klaus, A., and the Expedition 320/321 Scientists, *Proc. IODP, 320/321*: Tokyo (Integrated Ocean Drilling Program Management International, Inc.). doi:10.2204/iodp.proc.320321.203.2012

²Department of Oceanography, Texas A&M University, College Station TX 77843, USA. Correspondence author: mlyle@ocean.tamu.edu

³Integrated Ocean Drilling Program, Texas A&M University, 1000 Discovery Drive, College Station TX 77845-9547, USA.

⁴Institut für Geowissenschaften, Christian-Albrechts-Universität zu Kiel, Olshausenstrasse 40, 24098 Kiel, Germany.

⁵Center for Marine Environmental Sciences (MARUM), University of Bremen, PO Box 330440, 28334 Bremen, Germany.

⁶IFM-GEOMAR, Leibniz Institute of Marine Sciences at University of Kiel, Wischhofstrasse 1-3, D-24148 Kiel, Germany.

⁷Institute of Observational Research for Global Change (IORGC), Japan Agency for Marine-Earth Science and Technology, 2-15 Natsushima-Cho, Yokosuka 237-0061, Japan.

⁸Institute of Low Temperature Science, Hokkaido University, N19W8, Kita-Ku, Sapporo 060-0819, Japan.

Abstract

We used X-ray fluorescence (XRF) scanning on Site U1338 sediments from Integrated Ocean Drilling Program Expedition 321 to measure sediment geochemical compositions at 2.5 cm resolution for the 450 m of the Site U1338 spliced sediment column. This spatial resolution is equivalent to ~2 k.y. age sampling in the 0–5 Ma section and ~1 k.y. resolution from 5 to 17 Ma. Here we report the data and describe data acquisition conditions to measure Al, Si, K, Ca, Ti, Fe, Mn, and Ba in the solid phase. We also describe a method to convert the data from volume-based raw XRF scan data to a normalized mass measurement ready for calibration by other geochemical methods. Both the raw and normalized data are reported along the Site U1338 splice.

Introduction

A primary objective of the Integrated Ocean Drilling Program (IODP) Pacific Equatorial Age Transect (PEAT) project is to produce continuous records that track the effects of climate change in the equatorial Pacific with enough detail to resolve orbitally forced climate cycles. A significant part of climate change is recorded by variability in the chemical composition of sediments, but this information typically is hard to extract at a reasonable cost.

X-ray fluorescence (XRF) scanning is potentially an economical way to extract the chemical data—it is an X-ray optical technique that can measure most major elements and some minor ones in ~20–30 s per measurement. This method can be used to gather chemical data at vertical spacing similar to that at which physical properties data are gathered (e.g., Westerhold and Röhl, 2009). These chemical measurements can augment physical properties measurements to study cyclostratigraphy, and if calibrated, XRF scan data can be used to understand the long-term evolution of biogeochemical cycles.

In this data report, we present the results of XRF scanning on the spliced sedimentary section of PEAT Site U1338 and describe a basic technique to normalize and calibrate the data for further geochemical study. Both the raw and normalized data along the splice are presented in tables. Data at this sampling resolution for the first time allows the study of geochemical cycles for long periods in the Miocene and of how biogeochemical changes are



associated with long-term changes in global climate.

Site U1338 (Fig. F1; 2°30.469'N, 117°58.178'W; 4200 m water depth) is on 18 Ma ocean crust buried by ~400 m of pelagic sediment (see the “Site U1338” chapter [Expedition 320/321 Scientists, 2010b]). The sediment drapes over topography so that the ~200 m abyssal hill relief on basement is still visible despite the 400 m of sediment cover (Tominaga et al., 2011).

Site U1338 has the characteristic variations in sedimentary calcium carbonate content that result in the common seismic stratigraphy that is found throughout the equatorial Pacific region east of Hawaii (Mayer et al., 1985, 1986; see the “Site U1338” chapter [Expedition 320/321 Scientists, 2010b]; Tominaga et al., 2011). It has been a long-standing scientific problem to understand what forcing mechanisms and associated variations in global geochemical cycles caused the carbonate cycles that in turn caused the common seismic horizons across the equatorial Pacific. XRF scanning potentially can determine calcite contents with sufficient detail to better understand both the links between physical properties and sediment carbonate contents and why sedimentary carbonate varied throughout the eastern equatorial Pacific.

XRF studies of biogeochemically active elements Ca, Si, and Ba also can be used to understand changes in productivity and can be compared to changes in preservation to better understand changes in the carbon cycle. XRF scanning also can measure aluminosilicate elements (Al, K, and Ti) to understand dust deposition in the equatorial Pacific, whereas measurements of the redox-sensitive elements Fe and Mn can be used to study changes in the sedimentary redox environment and hydrothermal activity. Dymond (1981) shows how chemical data can be used to discern sediment processes in the eastern equatorial Pacific.

X-ray fluorescence analytical technique

X-ray fluorescence is an analytical technique that uses the characteristic fluorescence of elements exposed to high-energy X-ray illumination as a means to estimate a sample’s chemical composition. High-energy X-ray photons eject inner-shell electrons from atoms being illuminated by the X-rays (Jansen et al., 1998). Outer shell electrons in higher energy levels then occupy these lower energy levels, releasing the excess energy as characteristic XRF for each element. The intensity of the fluorescence from a

sample can be used to determine the abundance of different elements.

XRF is a volume and not a mass measurement, however. A conventional chemical analysis measures the amount of an element in a standard mass of total material; a sample with 8 wt% Fe has, for example, 8 g Fe per 100 g sample. For XRF, in contrast, the X-ray source illuminates a certain volume of sediment, and the amount of X-rays returned in part depends on the mass of sediment in that volume. Low atomic weight elements emit lower energy X-rays than high atomic weight elements, and these low-energy X-rays are more easily absorbed by other elements as they pass out of the sample. For this reason, light elements have a smaller characteristic emission volume than heavy elements (Tjallingii et al., 2007), causing problems if the sample is not homogeneous.

For unconsolidated sediments, part of the illuminated volume is occupied by pore space, so that the volume XRF return is less than that from a pure solid. Because scanning XRF is a volume measurement, there is a correlation between XRF-scan raw X-ray peak areas and wet bulk density (Fig. F2). Low wet bulk density marks samples with high porosity and low solid mass per sample, in contrast to samples with high bulk density. The volume effect most strongly affects the most abundant elements in the samples—in the case of carbonate-rich equatorial Pacific sediments, the correlation is best found with Ca.

In order to remove the volume effect, the data must be normalized before calibration. The normalization method used in this paper (normalized median-scaled sums) is described in “Data reduction methods for later calibration: normalized median-scaled method” later in this data report.

Data acquisition methods

Data in this data report were acquired at the IODP Gulf Coast Repository in College Station, Texas (USA) (odases.tamu.edu/research-facilities/xrf-request/), using a third generation Avaatech XRF scanner with a Canberra X-PIPS SDD, model SXD 15C-150-500 150 eV resolution X-ray detector. The XRF scanner is configured to analyze split sediment core halves for elements between Al and U in the periodic table. The X-ray tube and detector apparatus is mounted on a moving track so that multiple spots at different depths can be analyzed on a split core during the scanning run and multiple scans with different settings can be automatically programmed (Richter et al., 2006). Many parameters are controlled by the operator. For example, there are controls for X-

ray tube current, voltage, measurement time (live time), X-ray filters used, and area of X-ray illumination. The downcore position step is precise to 0.1 mm.

For Site U1338 XRF scans, sample spacing along each core section was set at 2.5 cm intervals and separate scans at two voltages were used. One scan was performed at 10 kV for the elements Al, Si, S, Cl, K, Ca, Ti, Mn, and Fe, and a repeat scan was performed at 50 kV for Ba. The voltage used for elements measured is determined by the energy needed to excite the appropriate characteristic X-rays. The X-ray illumination area was set at 1.0 cm in the downcore direction and 1.2 cm in the cross-core direction, and the scan was run down the center of the split core half (6.8 cm total diameter). Both scans were done with an X-ray tube current of 2 mA. Settings used for Site U1338 10 kV XRF scans are 2 mA tube current, no filter, and a detector live time of 20 s; for the 50 kV scan the settings are 2 mA current, Cu filter, and a detector live time of 10 s.

After consultations with colleagues in Bremen, Germany, we now use lower power to preserve tube life and reduce possibility of peak overlap problems. The raw X-ray peak areas are proportional to the power applied. Figure F3A is a comparison of data from XRF scans done at the Gulf Coast Repository on Section 321-U1337A-12H-2 using two different X-ray tube currents at 10 kV. For all elements the peak area measured is proportional to the tube current multiplied by the count time. The slope for each elemental data set is near the slope of 0.375 expected from the power-time ratios between the two runs. Figure F3B is a similar comparison between two different Avaatech scanners with different detectors: the Bremen MARUM XRF3 scanner (then equipped with a Canberra SXP 5C-200-1500 V2 200 eV resolution detector) versus the Gulf Coast Repository scanner (Canberra SXD 15C-150-500 150 eV resolution detector) on the Eocene/Oligocene boundary section of Hole U1333C (Sections 320-U1333C-14H-4 and 14H-5). The raw data in this comparison are also linearly proportional to power, although different sensitivities of the SXP versus SXD X-ray detectors add an additional linear factor to the count differences. In each example, there is more variability within the light element (Al) measurement where counts are low and air absorption of the low-energy X-rays is more significant. Nevertheless, the different scanners detect a similar chemical signal.

Prior to scanning, each core section was removed from refrigeration at least 2 h before scanning and was covered ~15 min before the scanning with 4 μ m thick Ultralene plastic film (SPEX Centriprep, Inc.). Ultralene film protects the detector face from becom-

ing sediment covered and contaminated during the scan. It is important to wait until the core sections warm to room temperature before putting the film on them. Plastic film placed over cool core sections can lead to water condensation on the film and severely reduce light element XRF peak areas by absorbing the emitted low-energy X-rays. We observed in one test a 25%–50% reduction in Ca peak area comparing a cold-run core section to the same section after it was allowed to warm and the Ultralene was replaced. The difference in measured peak area between the warm and cold core was not constant in this particular test but increased downcore on the cold core as the condensation continued to form. Also see Tjallingii et al. (2007) for a discussion of water on light element XRF intensities.

Only core sections along the continuous spliced section of Site U1338 were analyzed, not every core section recovered at the site. We XRF-scanned every archive core half in the Site U1338 splice table (see Table T24 in the “Site U1338” chapter [Expedition 320/321 Scientists, 2010b]). If the splice transferred from one hole to the next in the middle of a section, we ran both entire sections. Therefore, most jump points in the splice have significant overlap. In a few cases where the splice was being revised (J. Dickens, pers. comm., 2011) we also scanned additional sections to help determine the best splice revision. All data gathered, including the overlaps, are included in Table T1. Table T2 has only the data following the published Site U1338 splice (see Table T24 in the “Site U1338” chapter [Expedition 320/321 Scientists, 2010b]), with minor revisions where the meters composite depth (mcd) depths did not match at the tabulated splice point and a revision between 40 and 45 mcd (core composite depth below seafloor [CCSF], method A [overlapping]; see the “Methods” chapter [Expedition 320/321 Scientists, 2010a]) where a mismatch was found by Dickens. Table T2 contains both the raw and normalized median-scaled (NMS) reduced data, described below.

Data reduction methods for later calibration: normalized median-scaled method

Data reduction was achieved through a simple two-step method: (1) data were scaled by the median shipboard-measured bulk sediment elemental composition to scale the elemental peak areas into typical ranges of sediment composition, and (2) scaled components were then summed and normalized to 100% to eliminate variability caused by differences

in porosity or cracks. This method of data reduction has a few similarities and several differences with that of Weltje and Tjallingii (2008). Weltje and Tjallingii (2008) normalize the peak areas first and then log transform the peak areas to reduce the range between major and minor XRF-emitters, like our median-scaling step. Finally, they solve a matrix of XRF element/element ratios for composition. The Weltje and Tjallingii (2008) approach has the advantage of being more global and developed from first principles, but it suffers from complexity and is not easily adapted. The advantage of the NMS technique is that it can be quickly implemented, and the calibration step can be used to determine if a more detailed approach is needed.

Sample scaling

Sample scaling is needed to better match the range of XRF peak area measurements to the range of chemical composition along the scan. Without scaling, normalized peak areas can be dominated by effects of one element.

For an elemental scaling S_e ,

$$S_e = \text{Med}\%_e \times (\text{PeakArea}_e / \text{PeakArea}_{e,\text{med}}),$$

where $\text{Med}\%_e$ is the median weight percent of a sedimentary component (e.g., for Fe, we used the oxide Fe_2O_3 , and for Ca, CaCO_3). PeakArea_e is the measured elemental peak area in a sample, and $\text{PeakArea}_{e,\text{med}}$ is the median peak area over the data set. There may be errors in absolute scaling because the chemical analyses are far fewer than the XRF sampling. The raw CaCO_3 data, for example, scales from 0% to ~120%. However, the normalizing step reduces the total range to between 0% and 100%, and the calibration step correlating the scaled data to ground-truth chemical analyses produces a linear correlation that does a final adjustment to the percentage data.

Scaling the raw peak areas was done because the production of characteristic X-rays of different elements does not scale linearly with elemental ratios in the sample. Scaling to the total summed peak area was rejected because scaling to raw peak area strongly overweights Ca in the carbonate-rich sediment column of Site U1338 and is a significant cause of non-linearities in later calibration. Scaling to total peak area is effectively equivalent to scaling to Ca peak area, as is shown by comparing Ca proportions in the two scaling schemes. Median peak area of Ca is 95% of summed total median peak area, whereas median CaCO_3 is 76% of the summed shipboard chemical analyses. The raw peak area Ca/Si ratio is 38.5, whereas the ratio of median $\text{CaCO}_3/\text{SiO}_2$ from ship-

board inductively coupled plasma-atomic emission spectroscopy (ICP-AES) analyses is 4.9. Summing to raw peak areas thus creates a burden that must be removed by the calibration step, whereas scaling to median values reduces the problem.

We scaled each element independently to a median of the compositional data from shipboard ICP-AES analyses (see the “Site U1338” chapter [Expedition 320/321 Scientists, 2010b]). Although the shipboard compositional data set is a much smaller sample set than the XRF scan data, it is appropriate for scaling as long as the compositional data set is a reasonable representation of the total range of composition. The scaling step could also be done with a generic average for the sediment type being studied if chemical data were not available. The use of a different “type” compositional analysis to scale the median value will change the ultimate NMS value and will then potentially change the slope of the calibration line to convert from NMS to calibrated percent. It is thus important to use the same scaling values within a common calibration.

Normalizing sample composition to 100%

Ideally, the sum of all sediment components should be 100% if all major elements are measured and they are properly converted to the appropriate sedimentary components (e.g., Ca is represented in the sediment by the sedimentary component CaCO_3 , not CaO). However, the XRF-scaled sum of components is often much lower than 100% near the top of the section where porosity is high and dry sample mass in the scan area is low. We used the following components for our data set: Al_2O_3 , SiO_2 , K_2O , CaCO_3 , TiO_2 , MnO , Fe_2O_3 , and BaSO_4 . From the shipboard chemical analyses, these components sum to a median of 94.7 wt% and adequately represent all sediment components. In contrast, the high-porosity upper 50 m of Site U1338 has a median of 67 wt% for the raw sum of components and a range from <20% to ~100%. Clearly, the raw sum has significant noise and is affected by the sediment water content.

The normalization procedure is basic—multiply each component by $100/(\text{raw sum})$ to bring the total sum of components to 100%, or

$$\text{NMS}_c = C \times 100/(\text{raw sum}),$$

where NMS_c is the normalized median-scaled value for the component and C is the median-scaled value of the component.

Normalization does a good job of removing the volume versus mass XRF effect. Near the surface of the sediment column, the major cause of low sums of

median-scaled data is the porosity effect. Deeper in the sediment section, however, the raw sum (and raw peak areas) are often variable because the sediment is stiffer and the core surface is cracked or sufficiently uneven that the X-ray detector assembly lands imperfectly (Fig. F4). Normalization minimizes this high-frequency noise. Figure F4 shows the raw median-scaled CaCO_3 and the NMS CaCO_3 in a deeper section of the Site U1338 splice (Table T2). Scaling and normalization reduced what appears to be noise in the measurement and made the total range more similar to the variability in the low-resolution CaCO_3 record (Lyle and Backman, submitted).

The scaling and normalization process in this data report provides a way to develop a quantitative estimate of sediment concentration based on XRF scans. However, one should always be aware that XRF estimates can have significant errors if the model of sediment composition used is seriously awry (e.g., that the “type” sediment composition used is significantly different from actual sediment composition). Another source of significant error can occur if the model sediment components don’t match those of the sediment or if a major element found in the sediments is not included in the model. However, despite these issues, NMS data are significantly better to study the changes in sediment composition than raw XRF peak area. Raw peak area data can have even larger relative errors resulting from significant differences in porosity between sediment layers or from technical problems landing the detector on a flat sediment surface.

Example calibration of data: BaSO_4

A final step—calibration with chemical analyses of the sediments—is required in order to properly estimate chemical composition with XRF. Figure F5 illustrates the basic process with shipboard Ba data, comparing the XRF BaSO_4 estimate from the preliminary linear calibration with the shipboard measurements. The shipboard data set is not ideal for this calibration because the shipboard and XRF data were often measured on different holes but matched by the common meters composite depth used to build the splice. Nonlinear distortions of adjacent sediment columns, either by coring or local sedimentation variability, add noise to the calibration by matching samples at different sediment horizons (Hagelberg et al., 1995). Compositional differences may actually exist between the shipboard ICP-AES and XRF NMS data that we used for the initial test

calibrations. Also, we did not have a sufficient number of samples to reserve some for a test data set to determine errors. Nevertheless, the correlation between the shipboard ICP-AES data and XRF Ba data is reasonably good and will be improved by measuring more samples along the splice.

A better example calibration exists for CaCO_3 data (Lyle and Backman, submitted). Lyle and Backman use an extensive discrete CaCO_3 data set to calibrate an XRF CaCO_3 estimate. Only half of the data are used for the calibration. A reserved half of the data set is used to assess the quality of the calibration. Reserving data allowed Lyle and Backman to show that the CaCO_3 estimate agreed with the measured CaCO_3 by ± 5 wt% (1 standard deviation).

Results and discussion

One of the important uses of XRF scanning is to be able to produce high-resolution data sets of chemical composition for long time spans (e.g., the 18 m.y. sediment record at Site U1338). Figure F6 shows NMS time series of CaCO_3 and SiO_2 . These two components average ~90% of the total sediment composition. Multiple intervals of low carbonate at Site U1338 are marked by tan bars on Figure F6. Each of these intervals have high SiO_2 , caused by either the dissolution loss of carbonate from the sediment column or by the very fast deposition of an SiO_2 -rich sediment component, like the late Miocene–Pliocene diatom mat deposits found in the eastern equatorial Pacific (Kemp and Baldauf, 1993; Expedition 320/321 Scientists, 2010b). One of the primary tasks of postexpedition studies is to understand how primary productivity and dissolution during early diagenesis have shaped the composition of the sediment column. Based on an average sedimentation rate of 25–30 m/m.y. below 60 revised meters composite depth (rmcd) in Site U1338 (see the “Site U1338” chapter [Expedition 320/321 Scientists, 2010b]) large-scale low weight percent CaCO_3 transients are spaced a million or more years apart. Smaller scale CaCO_3 variability is also observed at all the typical orbital forcing periods—400 to 19 k.y.

One way to study the aluminosilicate signal is with an aluminosilicate element like Ti. Because of low levels of aluminosilicates in the biogenic-rich equatorial Pacific sediments, it is more appropriate to use Ti than Al, because sufficient Al can be bound to bio- SiO_2 to cause an appreciable Al signal, especially at intervals in the sediment column where bio- SiO_2 was initially deposited at the seafloor but then partly dissolved during early diagenesis (Dymond et al., 1997). Figure F7 is a plot of TiO_2 and SiO_2 NMS concentra-

tions along the Site U1338 splice. The blue intervals mark intervals where SiO_2 is very high but TiO_2 is essentially zero. These sediment intervals are extremely rich in bio- SiO_2 . In the upper 60 m of the sediment column (tan interval), we observe higher TiO_2 associated with moderate SiO_2 , indicating relatively more clays. This interval marks the last 5 m.y. of the record as the site moved north of 1.3°N to its present position at 2.6°N . The increase in clay component may represent increased dissolution of bio- SiO_2 and CaCO_3 as sedimentation slowed down when Site U1338 moved away from the equatorial high-productivity zone or increased dust deposition as Site U1338 moves toward the Intertropical Convergence Zone. The interval of elevated Ti coincides with the upper section of core with lower sedimentation rates (12.7 m/m.y. versus 28.7 m/m.y. below; see Fig. F14 in the “Site U1338” chapter [Expedition 320/321 Scientists, 2010b]). Mass accumulation rates of TiO_2 , based on preliminary linear sedimentation rates, do not change with the increase in $\text{TiO}_2\%$. The lack in change of flux makes the biogenic sediment dissolution hypothesis the most probable cause for TiO_2 enrichment in the upper section, not higher dust deposition. Supporting this interpretation, the modern position of Site U1338 is well south of the dust maximum associated with the Intertropical Convergence Zone, 5° – 6° N since 5 Ma (Hovan, 1995).

Conclusions

We present scanning XRF data along the splice of Site U1338 (21,000 total sample measurements, with 17,000 along the splice) and show their use to explore the history of the equatorial Pacific productivity zone. We found that we could scan the Site U1338 splice in a reasonably short amount of time, averaging a little over 1 h apiece to scan ~250 sections along the Site U1338 splice for Al, Si, K, Ca, Ti, Mn, Fe, and Ba. Raw data are a volume measurement, however, and must be scaled, normalized, and eventually calibrated to make an estimate of sediment composition. The NMS data reduction process we describe helps to make correlations between raw peak areas and measured chemical compositions more linear so that calibration is easier. To achieve good results, care must be taken to choose a sediment compositional model (median composition and type of sediment components) that is similar to the sediments under analysis. Calibration is the final step to convert XRF scan data to a compositional estimate. Ideally, sufficient numbers of samples are

measured by other analytical methods that some of the data are left out of the calibration and can be used as check data.

Acknowledgments

We thank IODP Expedition 320/321 party members, IODP, and the IODP Gulf Coast Repository (GCR) for providing samples and data for this report and for all the effort they put in to properly collect and archive the Site U1338 sediment cores. We also acknowledge the Ocean Drilling and Sustainable Earth Sciences (ODASES) program at Texas A&M University for acquiring the Avaatech XRF scanner for the GCR. Scanning and analysis were paid for by a USAC postcruise grant and by NSF grant OCE-0962184 to ML and AOL. TW was funded by the Deutsche Forschungsgemeinschaft (DFG)-Leibniz Center for Surface Process and Climate Studies at the University of Potsdam.

References

- Dymond, J., 1981. Geochemistry of Nazca plate surface sediments: an evaluation of hydrothermal, biogenic, detrital, and hydrogenous sources. *In* Kulm, L.D., Dymond, J., Dasch, E.J., Hussong, D.M., and Roderick, R. (Eds.), *Nazca Plate: Crustal Formation and Andean Convergence*. Mem.—Geol. Soc. Am., 154:133–173.
- Dymond, J., Collier, R., McManus, J., Honjo, S., and Manzanini, S., 1997. Can the aluminum and titanium contents of ocean sediments be used to determine the paleoproductivity of the oceans? *Paleoceanography*, 12(4):586–593. doi:10.1029/97PA01135
- Expedition 320/321 Scientists, 2010a. Methods. *In* Pälike, H., Lyle, M., Nishi, H., Raffi, I., Gamage, K., Klaus, A., and the Expedition 320/321 Scientists, *Proc. IODP, 320/321*: Tokyo (Integrated Ocean Drilling Program Management International, Inc.). doi:10.2204/iodp.proc.320321.102.2010
- Expedition 320/321 Scientists, 2010b. Site U1338. *In* Pälike, H., Lyle, M., Nishi, H., Raffi, I., Gamage, K., Klaus, A., and the Expedition 320/321 Scientists, *Proc. IODP, 320/321*: Tokyo (Integrated Ocean Drilling Program Management International, Inc.). doi:10.2204/iodp.proc.320321.110.2010
- Hagelberg, T.K., Pisias, N.G., Mayer, L.A., Shackleton, N.J., and Mix, A.C., 1995. Spatial and temporal variability of late Neogene equatorial Pacific carbonate: Leg 138. *In* Pisias, N.G., Mayer, L.A., Janecek, T.R., Palmer-Julson, A., and van Andel, T.H. (Eds.), *Proc. ODP, Sci Results*, 138: College Station, TX (Ocean Drilling Program), 321–336. doi:10.2973/odp.proc.sr.138.116.1995
- Hovan, S.A., 1995. Late Cenozoic atmospheric circulation intensity and climatic history recorded by eolian deposition in the eastern equatorial Pacific Ocean, Leg 138.

- In Piasias, N.G., Mayer, L.A., Janecek, T.R., Palmer-Julson, A., and van Andel, T.H. (Eds.), *Proc. ODP, Sci. Results*, 138: College Station, TX (Ocean Drilling Program), 615–625. doi:10.2973/odp.proc.sr.138.132.1995
- Jansen, J.H.F., Van der Gaast, S.J., Koster, B., and Vaars, A.J., 1998. CORTEX, a shipboard XRF-scanner for element analyses in split sediment cores. *Mar. Geol.*, 151(1–4):143–153. doi:10.1016/S0025-3227(98)00074-7
- Kemp, A.E.S., and Baldauf, J.G., 1993. Vast Neogene laminated diatom mat deposits from the eastern equatorial Pacific Ocean. *Nature (London, U. K.)*, 362(6416):141–144. doi:10.1038/362141a0
- Lyle, M., and Backman, J., submitted. Data report: calibration of XRF-estimated CaCO₃ along the Site U1338 splice. In Pälke, H., Lyle, M., Nishi, H., Raffi, I., Gamage, K., Klaus, A., and the Expedition 320/321 Scientists, *Proc. IODP, 320/321*: Tokyo (Integrated Ocean Drilling Program Management International, Inc.).
- Mayer, L.A., Shipley, T.H., Theyer, F., Wilkens, R.H., and Winterer, E.L., 1985. Seismic modeling and paleoceanography at Deep Sea Drilling Project Site 574. In Mayer, L., Theyer, F., Thomas, E., et al., *Init. Repts. DSDP*, 85: Washington, DC (U.S. Govt. Printing Office), 947–970. doi:10.2973/dsdp.proc.85.132.1985
- Mayer, L.A., Shipley, T.H., and Winterer, E.L., 1986. Equatorial Pacific seismic reflectors as indicators of global oceanographic events. *Science*, 233(4765):761–764. doi:10.1126/science.233.4765.761
- Richter, T.O., van der Gaast, S., Koster, B., Vaars, A., Gieles, R., de Stigter, H.C., De Haas, H., and van Weering, T.C.E., 2006. The Avaatech XRF Core Scanner: technical description and applications to NE Atlantic sediments. In Rothwell, R.G. (Ed.), *New Techniques in Sediment Core Analysis*. Geol. Soc. Spec. Publ., 267(1):39–50. doi:10.1144/GSL.SP.2006.267.01.03
- Tjallingii, R., Röhl, U., Kölling, M., and Bickert, T., 2007. Influence of the water content on X-ray fluorescence core-scanning measurements in soft marine sediments. *Geochem., Geophys., Geosyst.*, 8(2):Q02004. doi:10.1029/2006GC001393
- Tominaga, M., Lyle, M., and Mitchell, N.C., 2011. Seismic interpretation of pelagic sedimentation regimes in the 18–53 Ma eastern equatorial Pacific: basin-scale sedimentation and infilling of abyssal valleys. *Geochem., Geophys., Geosyst.*, 12(3):Q03004. doi:10.1029/2010GC003347
- Weltje, G.J., and Tjallingii, R., 2008. Calibration of XRF core scanners for quantitative geochemical logging of sediment cores: theory and application. *Earth Planet. Sci. Lett.*, 274(3–4):423–438. doi:10.1016/j.epsl.2008.07.054
- Westerhold, T., and Röhl, U., 2009. High resolution cyclostratigraphy of the early Eocene—new insights into the origin of the Cenozoic cooling trend. *Clim. Past*, 5(3):309–327. doi:10.5194/cp-5-309-2009

Initial receipt: 2 September 2011

Acceptance: 1 November 2011

Publication: 29 February 2012

MS 320321-203

Figure F1. (A) Site map and (B) swath bathymetry map of Site U1338, located on 18 Ma crust formed at the East Pacific Rise (from the “Site U1338” chapter [Expedition 320/321 Scientists, 2010b]). Plate tectonic movement of the Pacific plate carried Site U1338 within 0.5° of the Equator between 13 and 8 Ma.

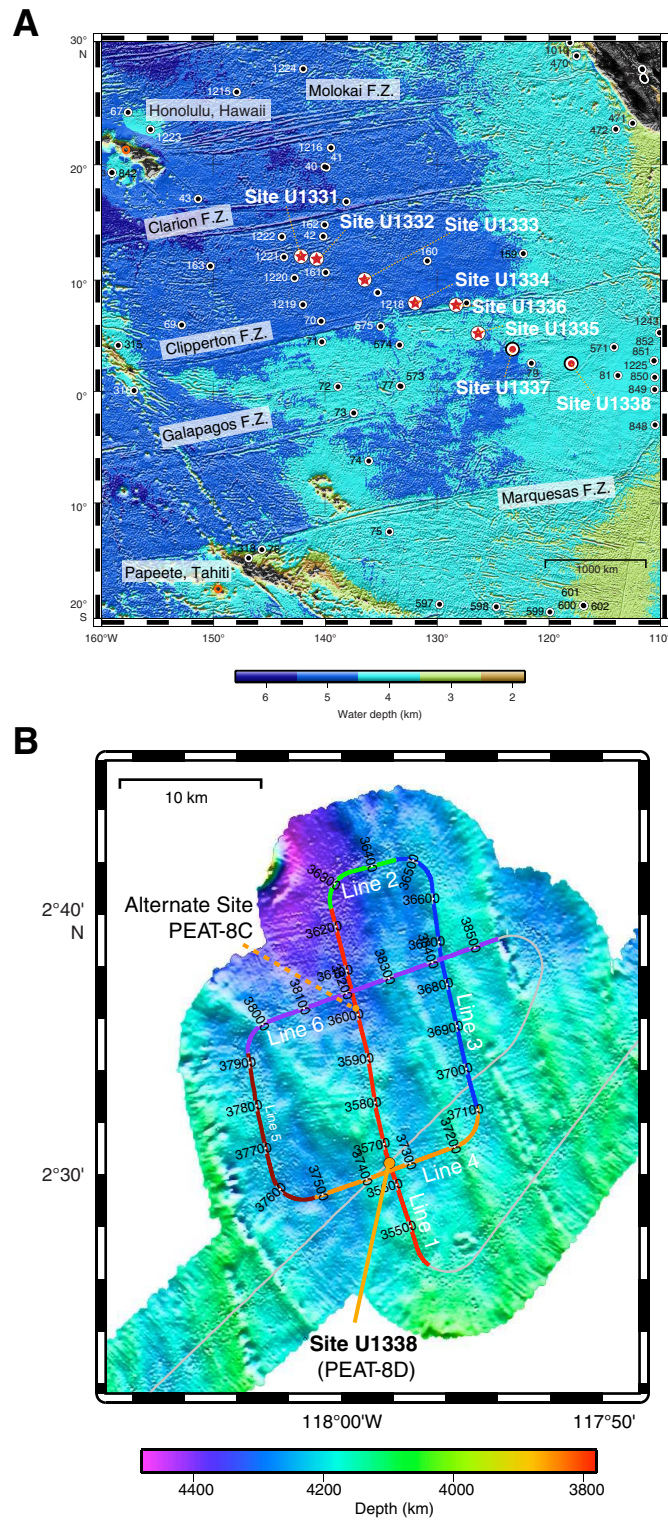




Figure F2. Raw sum of XRF-estimated sedimentary components compared to gamma ray attenuation (GRA) bulk density along the Site U1338 splice, reported in core composite depth below seafloor (CCSF), method B (compressed), showing the correlation between wet bulk density and the sum. The correlation exists because XRF scanning is a volume measurement and fluorescent X-ray returns depend on the total mass in the volume, which is related to the wet bulk density.

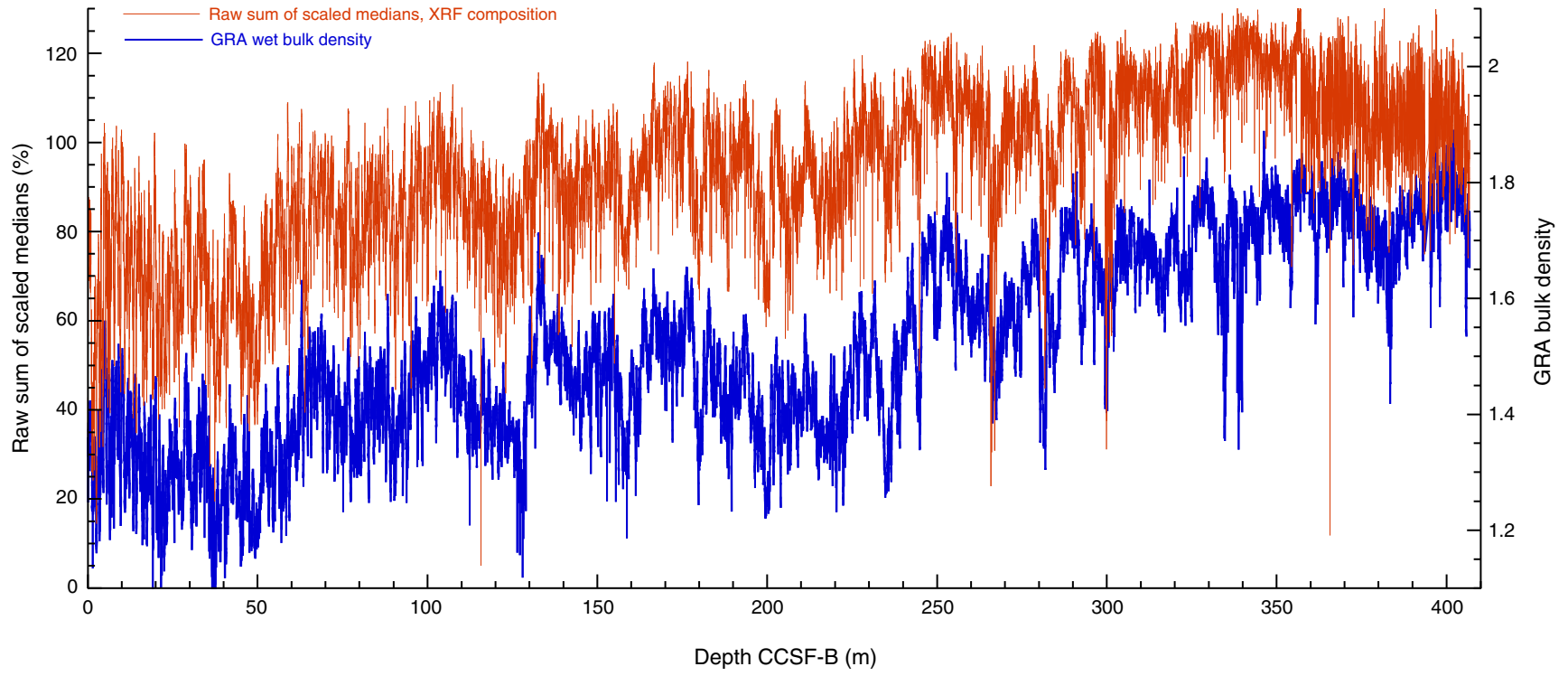




Figure F3. XRF scans run at two different tube currents to show the effect of power on peak areas and the effect of different detectors. A. Al and Fe scans at the Gulf Coast Repository (GCR) for Section 321-U1337A-12H-2 using 0.5 mA and 30 s live time (red line) vs. 2 mA and 20 s live time (blue line). Top plots in each shows a scatter plot of the individual samples. (Continued on next page.)

A GCR, 2 power settings

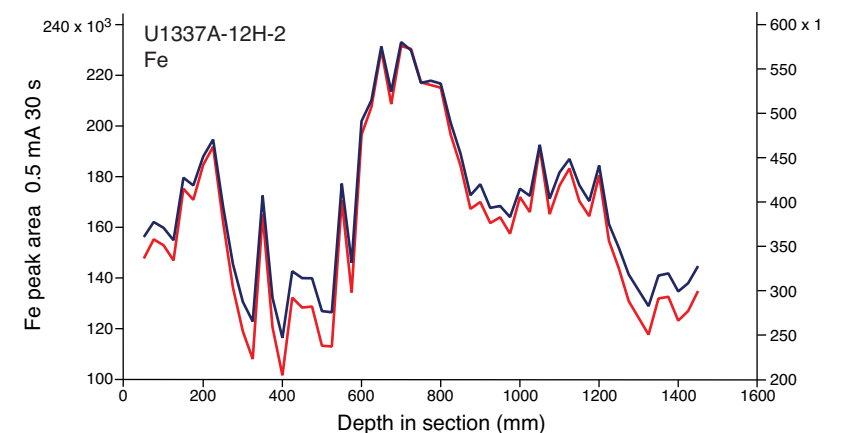
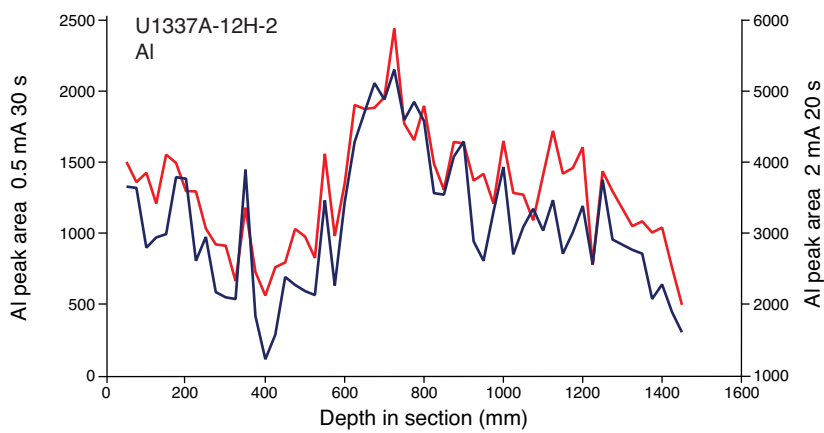
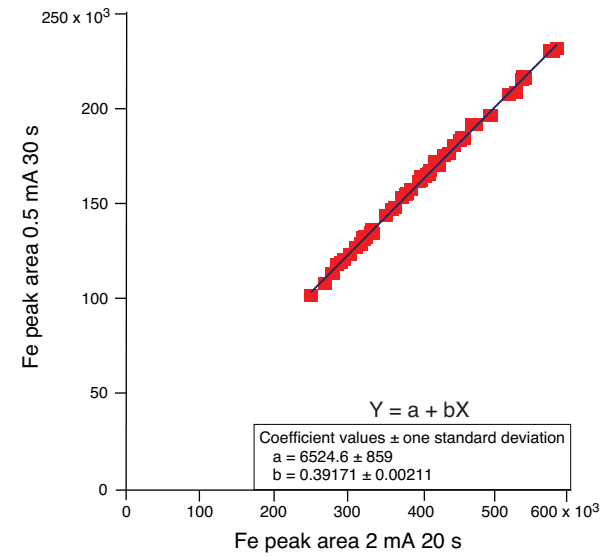
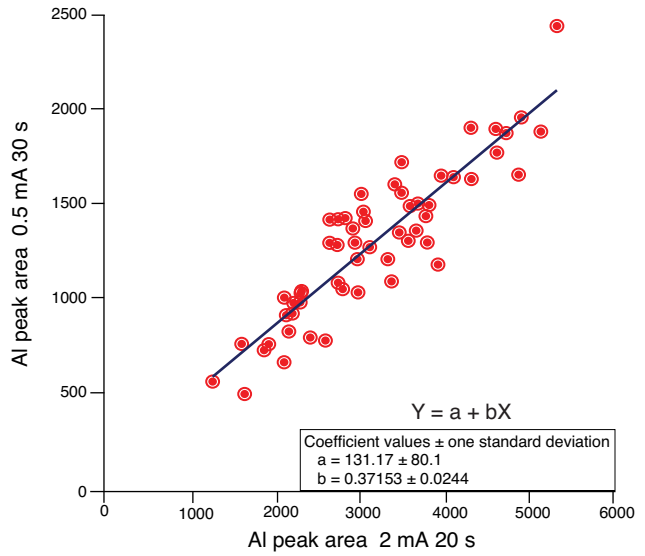




Figure F3 (continued). B. Al and Fe scans comparing the MARUM XRF 3 Avaatech scanner (Bremen; red line) with tube current of 0.12 mA and 20 s live time to the scans from the Gulf Coast Repository (GCR) Avaatech scanner using a tube current of 2 mA and 20 s live time (blue line). The two scanners have different generations of detectors with different sensitivity, but these differences did not appreciably affect the shape of the depth profiles. Top plots in each shows a scatter plot of the individual samples.

B GCR and MARUM, 2 power settings

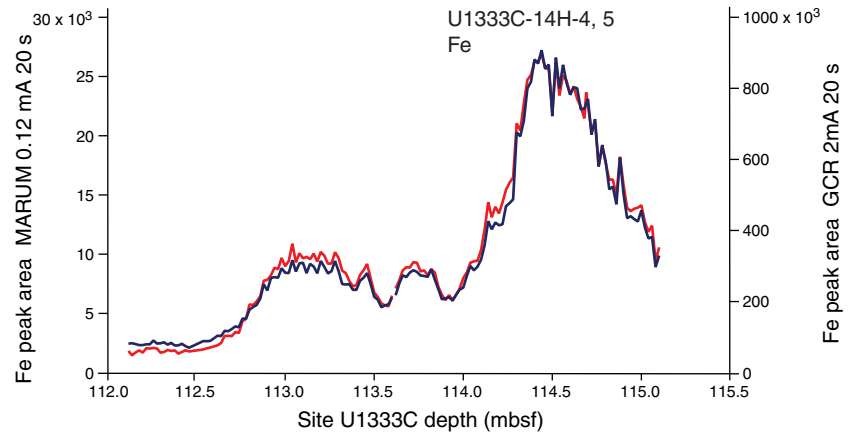
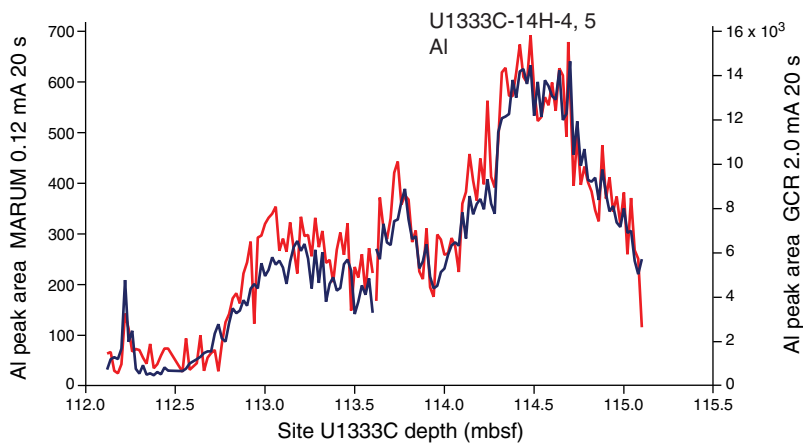
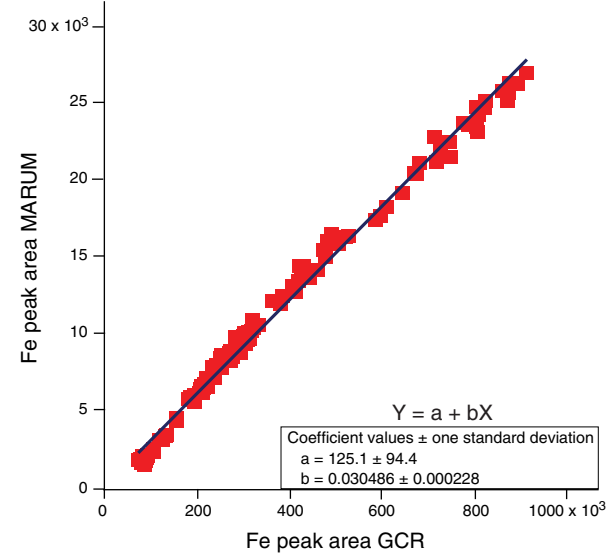
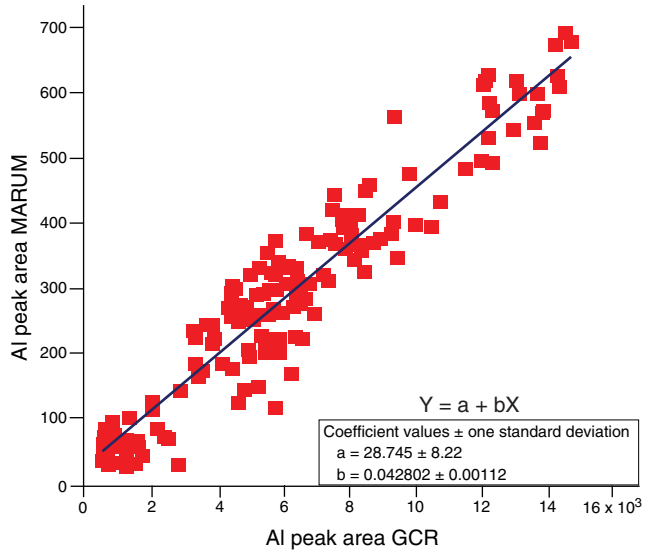




Figure F4. Comparison of raw median-scaled CaCO_3 data (green) with normalized (NMS) CaCO_3 estimate (blue), and discrete low-resolution CaCO_3 (J. Backman, unpubl. data) over the interval 400–420 mcd on the Site U1338 splice, shown in core composite depth below seafloor (CCSF), method A (overlapping). Raw data are significantly more variable because it is more difficult to land the XRF detector perfectly on the cracked and uneven surface of stiffer sediments. Normalizing the sum of components to 100% significantly removes the amount of sample-to-sample variability.

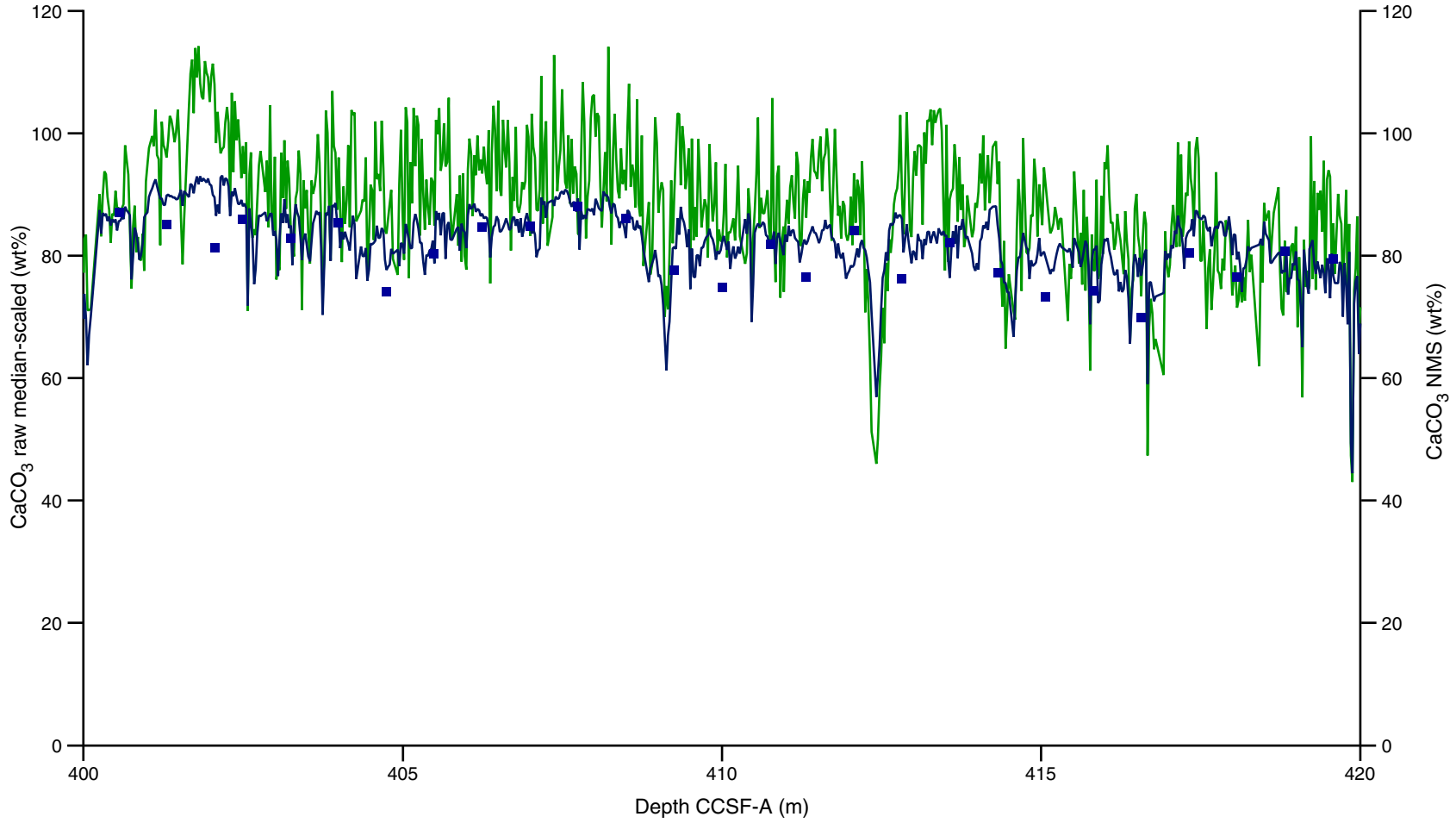




Figure F5. Comparison of the preliminary XRF-estimated BaSO_4 (red) to shipboard Ba (blue) measured by inductively coupled plasma–atomic emission spectroscopy (ICP-AES) expressed as BaSO_4 . Calibration graph is shown on right. Additional samples are needed for the calibration to better sample the range in Ba variability, but the match is encouraging. NMS = normalized.

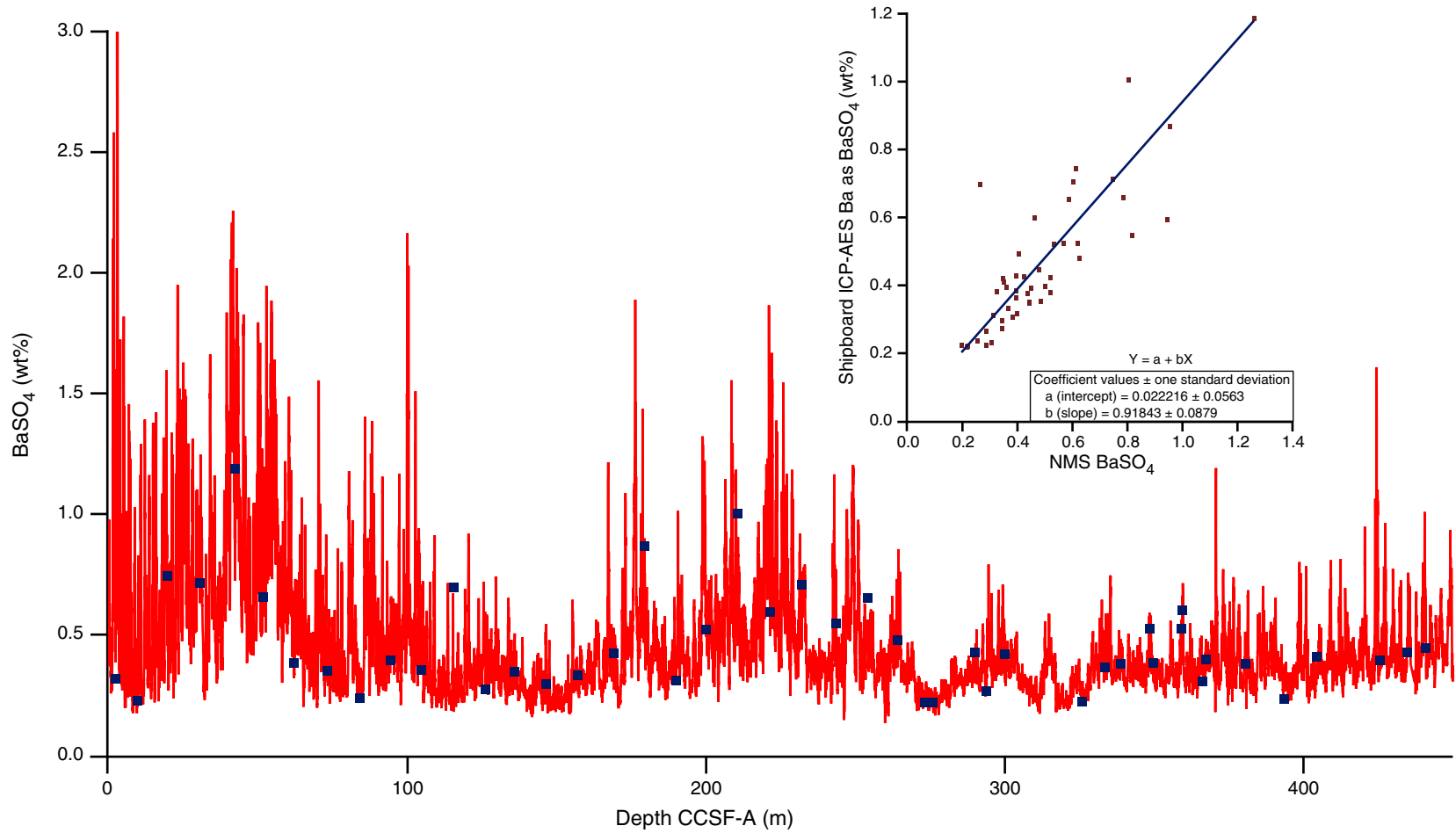




Figure F6. Comparison of uncalibrated normalized (NMS) $\text{CaCO}_3\%$ (red) and $\text{SiO}_2\%$ (blue) along the Site U1338 splice. Tan bands highlight prominent CaCO_3 lows/ SiO_2 highs. Much of the SiO_2 at Site U1338 is biogenic, so these represent either high bio-Si production and burial or high CaCO_3 dissolution. Higher resolution periodicity is apparent in the records and will be used for tuning sedimentation rates and to understand how the biogenic components respond to orbital forcing.

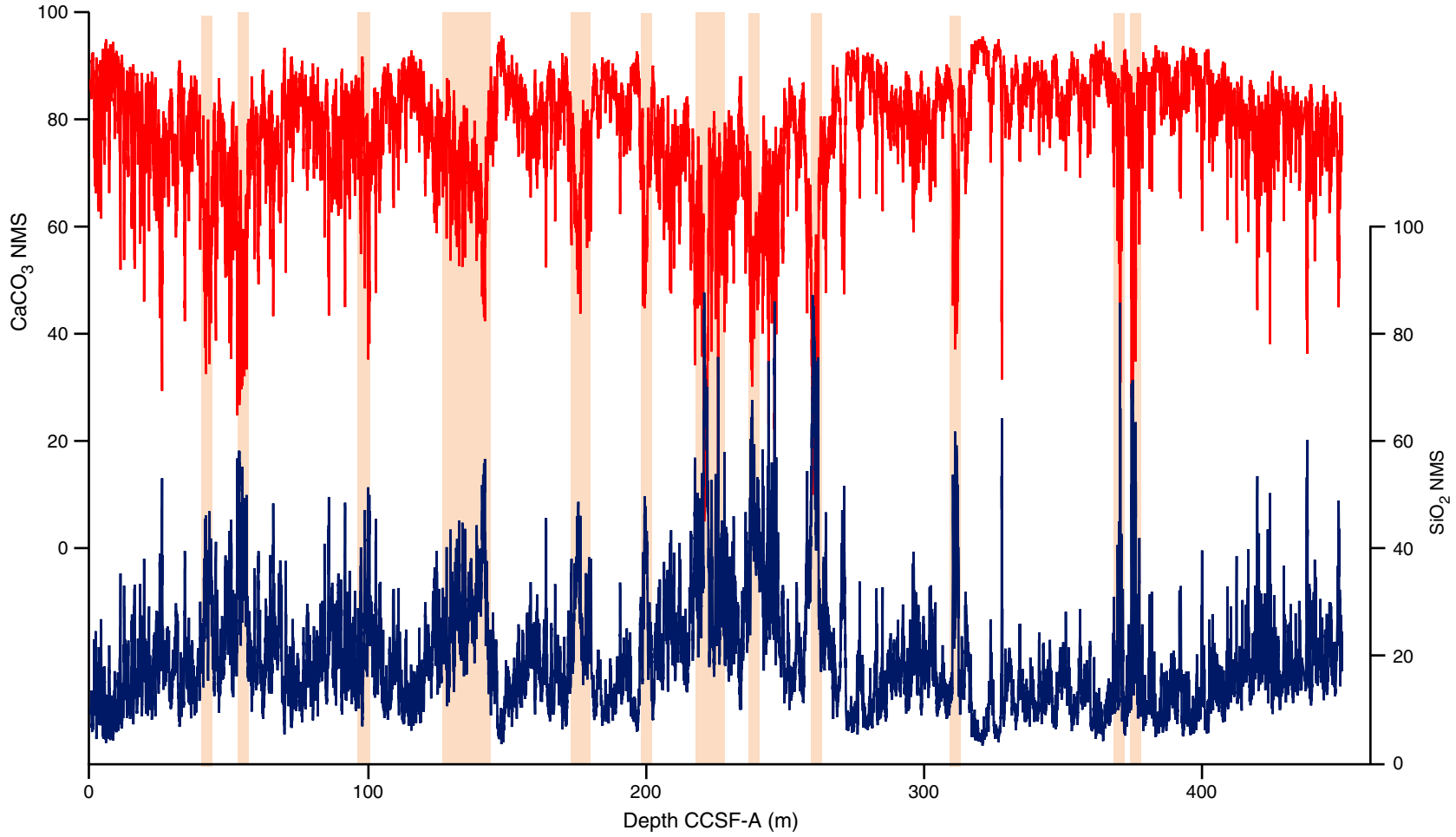




Figure F7. Comparison of uncalibrated normalized (NMS) $\text{TiO}_2\%$ (brown) and $\text{SiO}_2\%$ (blue) to discern clay (aluminosilicate) vs. biogenic contributions to the SiO_2 signal. Blue bands mark high biogenic- SiO_2 , determined when the SiO_2 is at a maximum but aluminosilicate elements like TiO_2 disappear. The brown band at the top of the sediment section is an area with moderate SiO_2 but relatively high amounts of TiO_2 , representing elevated aluminosilicates compared to the rest of the core. TiO_2 probably increases because of additional dissolution of bio- SiO_2 as sedimentation rates slow.

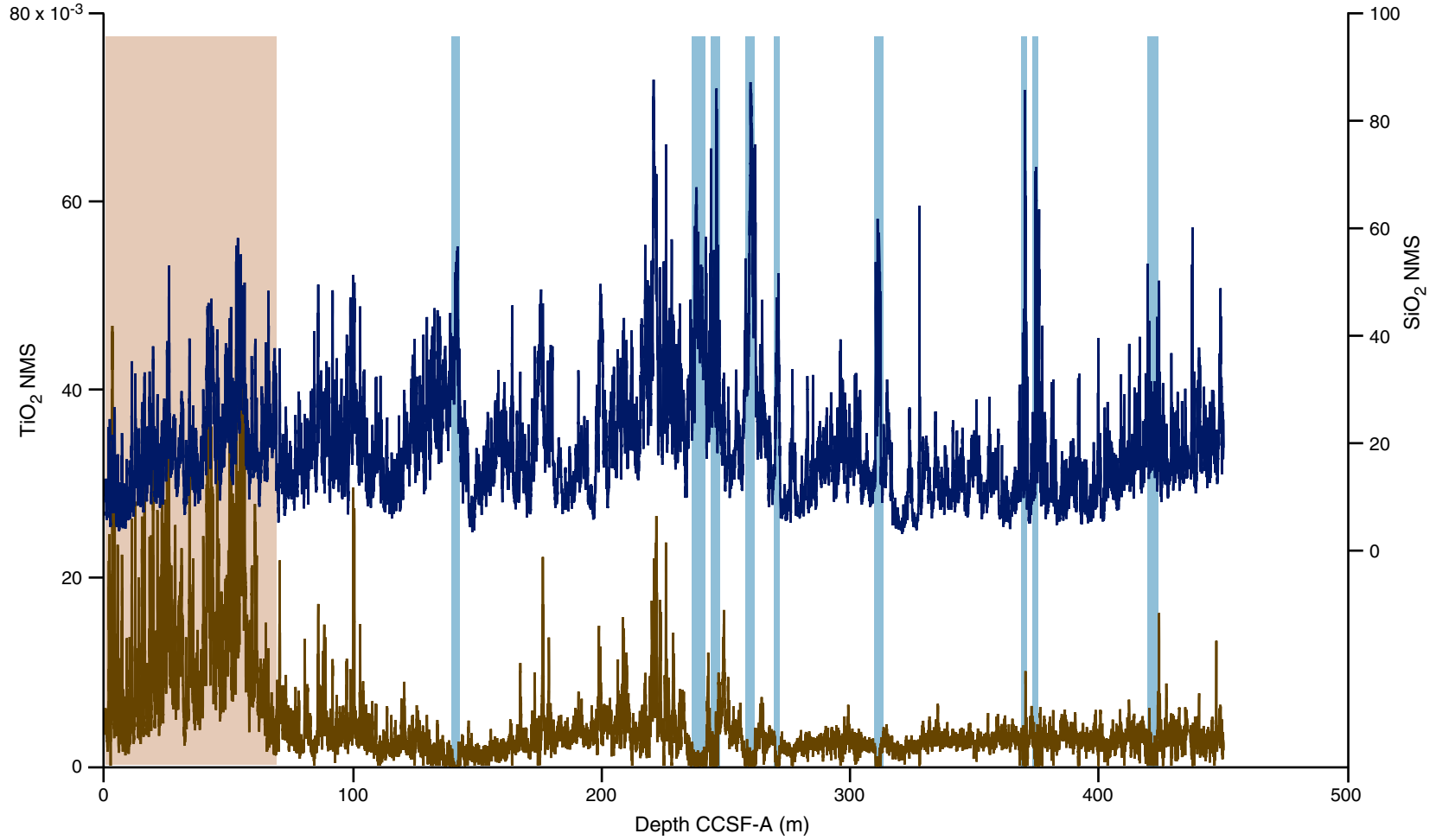




Table T1. Raw XRF scan peak area data for all scans on Site U1338, unspliced.

Core, section	Depth in section (mm)	Measurement date (2009)	Depth (mbsf/CSF-A [m])	Depth (mcd/CCSF-A [m])	Al area	Si area	S area	Cl area	K area	Ca area	Ti area	Mn area	Fe area	Ba area (50 kV scan)
321-U1338A-														
1H-1	25	29 Jul	0.025	0.065	-196	31,096	13,457	293,730	-1,343	2,258,381	1,320	65,711	50,683	3,398
1H-1	50	29 Jul	0.050	0.090	-98	39,489	27,680	771,065	7,437	2,914,316	3,180	114,737	90,042	12,199
1H-1	75	29 Jul	0.075	0.115	31	54,291	25,702	670,383	7,910	3,917,938	4,312	120,200	89,287	10,974
1H-1	100	29 Jul	0.100	0.140	-64	58,567	25,225	649,819	8,859	3,879,549	4,132	120,278	90,977	9,940
1H-1	125	29 Jul	0.125	0.165	261	74,200	21,599	559,320	8,642	5,529,714	5,545	150,111	90,424	10,158
1H-1	150	29 Jul	0.150	0.190	474	99,029	21,387	577,860	9,292	5,459,765	4,785	116,935	94,039	9,623
1H-1	175	29 Jul	0.175	0.215	294	79,255	22,413	611,799	7,209	5,622,123	5,203	148,228	87,932	9,972
1H-1	200	29 Jul	0.200	0.240	168	78,416	24,243	606,554	7,054	5,460,881	5,675	143,363	89,331	9,665
1H-1	225	29 Jul	0.225	0.265	633	106,394	21,727	570,990	7,893	5,467,310	4,459	149,993	93,019	10,382
1H-1	250	29 Jul	0.250	0.290	295	109,612	23,150	598,106	6,155	5,340,919	3,428	113,003	87,689	9,772
1H-1	275	29 Jul	0.275	0.315	165	79,464	20,977	557,697	6,094	6,125,817	4,628	215,611	96,548	10,461
1H-1	300	29 Jul	0.300	0.340	262	57,496	21,091	578,414	6,547	6,161,687	4,261	192,678	92,263	10,614
1H-1	325	29 Jul	0.325	0.365	397	55,628	23,413	622,942	6,987	5,875,783	5,078	45,705	87,897	9,471
1H-1	350	29 Jul	0.350	0.390	611	63,358	21,954	591,906	7,383	6,150,193	4,384	40,378	91,854	10,186
1H-1	375	29 Jul	0.375	0.415	448	59,072	21,785	612,824	5,672	5,821,063	4,437	30,007	78,209	8,369
1H-1	400	29 Jul	0.400	0.440	526	56,740	22,097	612,332	6,277	5,775,173	4,264	30,953	79,233	8,851
1H-1	425	29 Jul	0.425	0.465	515	59,134	21,841	627,211	5,879	6,045,124	4,183	33,817	79,555	8,692
1H-1	450	29 Jul	0.450	0.490	276	49,103	23,257	640,795	6,365	5,620,226	3,963	31,207	70,631	8,189
1H-1	475	29 Jul	0.475	0.515	474	40,776	24,811	707,600	5,090	5,065,880	3,154	36,204	68,976	8,088
1H-1	500	29 Jul	0.500	0.540	412	42,209	26,338	718,848	6,063	5,287,877	3,773	31,918	75,054	8,452
1H-1	525	29 Jul	0.525	0.565	250	43,704	23,015	668,223	5,078	5,400,234	2,662	26,998	69,963	7,515
1H-1	550	29 Jul	0.550	0.590	344	65,255	22,762	656,185	5,510	5,924,826	3,782	19,522	70,260	7,402
1H-1	575	29 Jul	0.575	0.615	508	55,367	23,779	649,213	4,293	5,533,030	3,150	22,116	69,223	7,482
1H-1	600	29 Jul	0.600	0.640	292	54,203	22,318	622,895	2,539	5,330,983	2,973	15,466	62,797	5,850
1H-1	625	29 Jul	0.625	0.665	551	69,327	21,772	604,146	3,248	6,307,831	2,841	21,300	70,224	6,139
1H-1	650	29 Jul	0.650	0.690	253	67,414	24,065	655,523	3,049	5,421,827	2,376	17,031	55,641	5,944
1H-1	675	29 Jul	0.675	0.715	360	57,532	22,015	617,115	4,382	5,934,125	2,834	56,416	67,879	6,751
1H-1	700	29 Jul	0.700	0.740	306	57,916	21,199	611,161	3,128	5,851,201	2,740	40,821	67,904	6,692
1H-1	725	29 Jul	0.725	0.765	620	62,461	20,340	571,223	4,724	6,091,732	2,762	50,170	66,785	6,742
1H-1	750	29 Jul	0.750	0.790	261	44,115	20,660	629,893	2,852	5,095,266	1,733	34,887	59,237	7,112
1H-1	775	29 Jul	0.775	0.815	325	49,114	18,640	574,651	1,430	5,803,417	1,901	26,677	62,104	6,532
1H-1	800	29 Jul	0.800	0.840	266	54,097	20,076	636,584	2,043	5,640,361	1,876	30,073	67,662	6,624
1H-1	825	29 Jul	0.825	0.865	110	48,609	22,560	622,630	1,103	4,894,580	2,253	39,294	59,105	6,967
1H-1	850	29 Jul	0.850	0.890	263	70,631	22,439	616,785	3,341	5,000,849	2,508	57,592	65,050	6,810
1H-1	875	29 Jul	0.875	0.915	646	77,556	21,123	596,848	4,157	6,044,992	3,010	33,031	76,096	6,822
1H-1	900	29 Jul	0.900	0.940	337	62,267	20,490	605,333	882	4,777,876	3,988	35,152	62,327	6,855
1H-1	925	29 Jul	0.925	0.965	47	58,742	24,689	670,855	3,681	4,745,994	1,546	26,640	63,732	6,243
1H-1	950	29 Jul	0.950	0.990	400	73,213	22,566	620,576	3,830	4,834,842	1,273	22,303	71,860	7,165
1H-1	975	29 Jul	0.975	1.015	350	73,781	21,954	611,750	5,517	5,119,603	2,019	23,729	70,781	7,286
1H-1	1,000	29 Jul	1.000	1.040	610	89,812	19,612	539,125	4,517	5,907,522	3,215	26,194	73,703	6,210
1H-1	1,025	29 Jul	1.025	1.065	544	81,524	20,710	568,607	5,489	5,312,686	2,855	37,549	69,539	6,541
1H-1	1,050	29 Jul	1.050	1.090	171	60,647	22,569	607,420	3,570	4,806,630	2,427	56,226	67,783	6,657
1H-1	1,075	29 Jul	1.075	1.115	-56	54,263	24,678	616,152	6,011	3,942,852	3,024	58,016	73,135	6,530

Overlaps of sections where the splice jumps to a different hole are shaded (tan = overlapping sections in splice, green = splice join). Al, Si, K, Ca, Ti, Mn, and Fe are from the 10 kV scan; Ba is from the 50 kV scan. Only a portion of this table appears here. The complete table is available in [ASCII](#) and in Microsoft Excel format (see RAWUNSPL.XLS in XRF in "Supplementary material").

Table T2. Spliced NMS, Hole U1338A. (Continued on next two pages.)

Core, section	Depth in section (mm)	Measurement date (2009)	Depth (mbsf/CSF-A [m])	Depth (mcd/CCSF-A [m])	Raw component sum (%)	Al area	Al median-scale	Al ₂ O ₃ NMS	Si area	Si median-scale	SiO ₂ NMS	S area
321-U1338A-												
1H-1	25	29 Jul	0.025	0.065	32.443	-196	0.000	0.000	31,096	3.04	9.38	13,457
1H-1	50	29 Jul	0.050	0.090	42.712	-98	0.000	0.000	39,489	3.86	9.04	27,680
1H-1	75	29 Jul	0.075	0.115	56.755	31	0.008	0.014	54,291	5.31	9.36	25,702
1H-1	100	29 Jul	0.100	0.140	56.684	-64	0.000	0.000	58,567	5.73	10.11	25,225
1H-1	125	29 Jul	0.125	0.165	79.203	261	0.069	0.087	74,200	7.26	9.16	21,599
1H-1	150	29 Jul	0.150	0.190	80.580	474	0.125	0.155	99,029	9.69	12.02	21,387
1H-1	175	29 Jul	0.175	0.215	80.788	294	0.078	0.096	79,255	7.75	9.60	22,413
1H-1	200	29 Jul	0.200	0.240	78.611	168	0.044	0.056	78,416	7.67	9.76	24,243
1H-1	225	29 Jul	0.225	0.265	81.680	633	0.167	0.205	106,394	10.41	12.74	21,727
1H-1	250	29 Jul	0.250	0.290	79.923	295	0.078	0.098	109,612	10.72	13.42	23,150
1H-1	275	29 Jul	0.275	0.315	87.682	165	0.044	0.050	79,464	7.77	8.87	20,977
1H-1	300	29 Jul	0.300	0.340	85.808	262	0.069	0.081	57,496	5.62	6.55	21,091
1H-1	325	29 Jul	0.325	0.365	80.863	397	0.105	0.130	55,628	5.44	6.73	23,413
1H-1	350	29 Jul	0.350	0.390	85.145	611	0.161	0.190	63,358	6.20	7.28	21,954
1H-1	375	29 Jul	0.375	0.415	80.249	448	0.118	0.148	59,072	5.78	7.20	21,785
1H-1	400	29 Jul	0.400	0.440	79.514	526	0.139	0.175	56,740	5.55	6.98	22,097
1H-1	425	29 Jul	0.425	0.465	83.140	515	0.136	0.164	59,134	5.78	6.96	21,841
1H-1	450	29 Jul	0.450	0.490	76.661	276	0.073	0.095	49,103	4.80	6.27	23,257
1H-1	475	29 Jul	0.475	0.515	68.939	474	0.125	0.182	40,776	3.99	5.79	24,811
1H-1	500	29 Jul	0.500	0.540	71.903	412	0.109	0.151	42,209	4.13	5.74	26,338
1H-1	525	29 Jul	0.525	0.565	73.274	250	0.066	0.090	43,704	4.28	5.83	23,015
1H-1	550	29 Jul	0.550	0.590	81.936	344	0.091	0.111	65,255	6.38	7.79	22,762
1H-1	575	29 Jul	0.575	0.615	76.084	508	0.134	0.176	55,367	5.42	7.12	23,779
1H-1	600	29 Jul	0.600	0.640	73.171	292	0.077	0.105	54,203	5.30	7.25	22,318
1H-1	625	29 Jul	0.625	0.665	87.105	551	0.146	0.167	69,327	6.78	7.79	21,772
1H-1	650	29 Jul	0.650	0.690	75.556	253	0.067	0.088	67,414	6.59	8.73	24,065
1H-1	675	29 Jul	0.675	0.715	81.516	360	0.095	0.117	57,532	5.63	6.90	22,015
1H-1	700	29 Jul	0.700	0.740	80.348	306	0.081	0.101	57,916	5.67	7.05	21,199
1H-1	725	29 Jul	0.725	0.765	83.993	620	0.164	0.195	62,461	6.11	7.27	20,340
1H-1	750	29 Jul	0.750	0.790	69.393	261	0.069	0.099	44,115	4.32	6.22	20,660
1H-1	775	29 Jul	0.775	0.815	78.685	325	0.086	0.109	49,114	4.80	6.11	18,640
1H-1	800	29 Jul	0.800	0.840	77.206	266	0.070	0.091	54,097	5.29	6.85	20,076
1H-1	825	29 Jul	0.825	0.865	67.264	110	0.029	0.043	48,609	4.75	7.07	22,560
1H-1	850	29 Jul	0.850	0.890	71.032	263	0.070	0.098	70,631	6.91	9.73	22,439
1H-1	875	29 Jul	0.875	0.915	84.829	646	0.171	0.201	77,556	7.59	8.94	21,123
1H-1	900	29 Jul	0.900	0.940	67.185	337	0.089	0.133	62,267	6.09	9.07	20,490
1H-1	925	29 Jul	0.925	0.965	66.351	47	0.012	0.019	58,742	5.75	8.66	24,689
1H-1	950	29 Jul	0.950	0.990	69.048	400	0.106	0.153	73,213	7.16	10.37	22,566
1H-1	975	29 Jul	0.975	1.015	72.707	350	0.092	0.127	73,781	7.22	9.93	21,954
1H-1	1,000	29 Jul	1.000	1.040	84.207	610	0.161	0.191	89,812	8.79	10.43	19,612
1H-1	1,025	29 Jul	1.025	1.065	76.006	544	0.144	0.189	81,524	7.97	10.49	20,710
1H-1	1,050	29 Jul	1.050	1.090	67.609	171	0.045	0.067	60,647	5.93	8.77	22,569
1H-1	1,075	29 Jul	1.075	1.115	56.223	-56	0.000	0.000	54,263	5.31	9.44	24,678
1H-1	1,100	29 Jul	1.100	1.140	45.720	-127	0.000	0.000	45,904	4.49	9.82	24,823
1H-1	1,125	29 Jul	1.125	1.165	62.460	4	0.001	0.002	79,860	7.81	12.51	24,486
1H-1	1,150	29 Jul	1.150	1.190	48.900	117	0.031	0.063	56,342	5.51	11.27	20,845
1H-1	1,175	29 Jul	1.175	1.215	54.956	182	0.048	0.088	79,743	7.80	14.19	30,302
1H-1	1,200	29 Jul	1.200	1.240	49.787	195	0.052	0.104	71,091	6.95	13.97	31,844
1H-1	1,225	29 Jul	1.225	1.265	54.761	104	0.027	0.050	74,635	7.30	13.33	25,977
1H-1	1,250	29 Jul	1.250	1.290	35.408	-331	0.000	0.000	45,485	4.45	12.57	31,332
1H-1	1,275	29 Jul	1.275	1.315	45.565	430	0.114	0.249	107,283	10.49	23.03	35,849
1H-1	1,300	29 Jul	1.300	1.340	26.109	-169	0.000	0.000	37,894	3.71	14.20	33,187
1H-1	1,325	29 Jul	1.325	1.365	33.589	-38	0.000	0.000	58,964	5.77	17.17	29,457
1H-1	1,350	29 Jul	1.350	1.390	39.756	-262	0.000	0.000	51,970	5.08	12.79	34,524
1H-1	1,375	29 Jul	1.375	1.415	35.315	-332	0.000	0.000	54,052	5.29	14.97	33,412
1H-1	1,400	29 Jul	1.400	1.440	43.730	-37	0.000	0.000	72,746	7.12	16.27	31,160
1H-1	1,425	29 Jul	1.425	1.465	46.225	336	0.089	0.192	88,308	8.64	18.69	27,293
1H-2	25	29 Jul	1.525	1.565	29.196	-146	0.000	0.000	59,620	5.83	19.98	26,096
1H-2	50	29 Jul	1.550	1.590	34.848	-349	0.000	0.000	42,906	4.20	12.04	32,993
1H-2	75	29 Jul	1.575	1.615	27.605	-272	0.000	0.000	26,424	2.58	9.36	32,931
1H-2	100	29 Jul	1.600	1.640	26.098	-251	0.000	0.000	30,607	2.99	11.47	32,628
1H-2	125	29 Jul	1.625	1.665	24.268	-176	0.000	0.000	35,143	3.44	14.17	30,839

Al, Si, K, Ca, Ti, Mn, and Fe, are from the 10 kV scan; Ba is from the 50 kV scan. Only a portion of this table appears here. The complete table is available in [ASCII](#) and in Microsoft Excel format (see NMSSPL.XLS in XRF in ["Supplementary material"](#)).

Table T2 (continued). (Continued on next page.)

Core, section	Depth in section (mm)	Cl area	K area	K median-scale	K ₂ O NMS	Ca area	Ca median-scale	CaCO ₃ NMS	Ti area	Ti median-scale	TiO ₂ NMS	Mn area	Mn median-scale
321-U1338A-													
1H-1	25	293,730	(1,343)	0.000	0.000	2,258,381	28.32	87.28	1,320	0.0011	0.0033	65,711	0.511
1H-1	50	771,065	7,437	0.172	0.403	2,914,316	36.54	85.55	3,180	0.0026	0.0060	114,737	0.893
1H-1	75	670,383	7,910	0.183	0.323	3,917,938	49.12	86.56	4,312	0.0035	0.0061	120,200	0.935
1H-1	100	649,819	8,859	0.205	0.362	3,879,549	48.64	85.82	4,132	0.0033	0.0059	120,278	0.936
1H-1	125	559,320	8,642	0.200	0.253	5,529,714	69.33	87.54	5,545	0.0045	0.0056	150,111	1.168
1H-1	150	577,860	9,292	0.215	0.267	5,459,765	68.46	84.95	4,785	0.0038	0.0048	116,935	0.910
1H-1	175	611,799	7,209	0.167	0.207	5,622,123	70.49	87.26	5,203	0.0042	0.0052	148,228	1.153
1H-1	200	606,554	7,054	0.163	0.208	5,460,881	68.47	87.10	5,675	0.0046	0.0058	143,363	1.115
1H-1	225	570,990	7,893	0.183	0.224	5,467,310	68.55	83.93	4,459	0.0036	0.0044	149,993	1.167
1H-1	250	598,106	6,155	0.143	0.178	5,340,919	66.97	83.79	3,428	0.0028	0.0034	113,003	0.879
1H-1	275	557,697	6,094	0.141	0.161	6,125,817	76.81	87.60	4,628	0.0037	0.0042	215,611	1.678
1H-1	300	578,414	6,547	0.152	0.177	6,161,687	77.26	90.04	4,261	0.0034	0.0040	192,678	1.499
1H-1	325	622,942	6,987	0.162	0.200	5,875,783	73.67	91.11	5,078	0.0041	0.0050	45,705	0.356
1H-1	350	591,906	7,383	0.171	0.201	6,150,193	77.11	90.57	4,384	0.0035	0.0041	40,378	0.314
1H-1	375	612,824	5,672	0.131	0.164	5,821,063	72.99	90.95	4,437	0.0036	0.0044	30,007	0.233
1H-1	400	612,332	6,277	0.145	0.183	5,775,173	72.41	91.07	4,264	0.0034	0.0043	30,953	0.241
1H-1	425	627,211	5,879	0.136	0.164	6,045,124	75.80	91.17	4,183	0.0034	0.0040	33,817	0.263
1H-1	450	640,795	6,365	0.147	0.192	5,620,226	70.47	91.92	3,963	0.0032	0.0042	31,207	0.243
1H-1	475	707,600	5,090	0.118	0.171	5,065,880	63.52	92.14	3,154	0.0025	0.0037	36,204	0.282
1H-1	500	718,848	6,063	0.140	0.195	5,287,877	66.30	92.21	3,773	0.0030	0.0042	31,918	0.248
1H-1	525	668,223	5,078	0.118	0.160	5,400,234	67.71	92.41	2,662	0.0021	0.0029	26,998	0.210
1H-1	550	656,185	5,510	0.128	0.156	5,924,826	74.29	90.67	3,782	0.0030	0.0037	19,522	0.152
1H-1	575	649,213	4,293	0.099	0.131	5,533,030	69.38	91.18	3,150	0.0025	0.0033	22,116	0.172
1H-1	600	622,895	2,539	0.059	0.080	5,330,983	66.84	91.35	2,973	0.0024	0.0033	15,466	0.120
1H-1	625	604,146	3,248	0.075	0.086	6,307,831	79.09	90.80	2,841	0.0023	0.0026	21,300	0.166
1H-1	650	655,523	3,049	0.071	0.093	5,421,827	67.98	89.97	2,376	0.0019	0.0025	17,031	0.133
1H-1	675	617,115	4,382	0.101	0.124	5,934,125	74.40	91.28	2,834	0.0023	0.0028	56,416	0.439
1H-1	700	611,161	3,128	0.072	0.090	5,851,201	73.36	91.31	2,740	0.0022	0.0027	40,821	0.318
1H-1	725	571,223	4,724	0.109	0.130	6,091,732	76.38	90.94	2,762	0.0022	0.0026	50,170	0.390
1H-1	750	629,893	2,852	0.066	0.095	5,095,266	63.89	92.06	1,733	0.0014	0.0020	34,887	0.271
1H-1	775	574,651	1,430	0.033	0.042	5,803,417	72.77	92.48	1,901	0.0015	0.0019	26,677	0.208
1H-1	800	636,584	2,043	0.047	0.061	5,640,361	70.72	91.60	1,876	0.0015	0.0020	30,073	0.234
1H-1	825	622,630	1,103	0.026	0.038	4,894,580	61.37	91.24	2,253	0.0018	0.0027	39,294	0.306
1H-1	850	616,785	3,341	0.077	0.109	5,000,849	62.70	88.27	2,508	0.0020	0.0028	57,592	0.448
1H-1	875	596,848	4,157	0.096	0.113	6,044,992	75.79	89.35	3,010	0.0024	0.0029	33,031	0.257
1H-1	900	605,333	882	0.020	0.030	4,777,876	59.91	89.17	3,988	0.0032	0.0048	35,152	0.274
1H-1	925	670,855	3,681	0.085	0.128	4,745,994	59.51	89.69	1,546	0.0012	0.0019	26,640	0.207
1H-1	950	620,576	3,830	0.089	0.128	4,834,842	60.62	87.79	1,273	0.0010	0.0015	22,303	0.174
1H-1	975	611,750	5,517	0.128	0.176	5,119,603	64.19	88.29	2,019	0.0016	0.0022	23,729	0.185
1H-1	1,000	539,125	4,517	0.105	0.124	5,907,522	74.07	87.96	3,215	0.0026	0.0031	26,194	0.204
1H-1	1,025	568,607	5,489	0.127	0.167	5,312,686	66.61	87.64	2,855	0.0023	0.0030	37,549	0.292
1H-1	1,050	607,420	3,570	0.083	0.122	4,806,630	60.27	89.14	2,427	0.0019	0.0029	56,226	0.437
1H-1	1,075	616,152	6,011	0.139	0.248	3,942,852	49.44	87.93	3,024	0.0024	0.0043	58,016	0.451
1H-1	1,100	668,021	4,239	0.098	0.215	3,198,341	40.10	87.71	1,676	0.0013	0.0029	38,598	0.300
1H-1	1,125	621,320	8,279	0.192	0.307	4,216,530	52.87	84.64	4,523	0.0036	0.0058	75,124	0.585
1H-1	1,150	510,676	3,212	0.074	0.152	3,360,285	42.13	86.16	4,060	0.0033	0.0067	35,604	0.277
1H-1	1,175	724,966	14,248	0.330	0.600	3,577,836	44.86	81.63	4,674	0.0038	0.0068	69,903	0.544
1H-1	1,200	721,878	7,842	0.182	0.365	3,306,120	41.45	83.26	3,188	0.0026	0.0051	34,079	0.265
1H-1	1,225	643,154	12,751	0.295	0.539	3,618,646	45.37	82.85	3,744	0.0030	0.0055	53,209	0.414
1H-1	1,250	753,138	12,815	0.297	0.838	2,292,403	28.74	81.18	4,540	0.0036	0.0103	39,202	0.305
1H-1	1,275	770,154	14,936	0.346	0.759	2,644,121	33.15	72.76	4,506	0.0036	0.0079	33,461	0.260
1H-1	1,300	805,380	14,758	0.342	1.309	1,581,744	19.83	75.96	5,125	0.0041	0.0158	39,551	0.308
1H-1	1,325	755,554	16,924	0.392	1.167	1,988,632	24.93	74.23	7,922	0.0064	0.0189	39,644	0.308
1H-1	1,350	814,134	19,003	0.440	1.107	2,530,553	31.73	79.81	7,434	0.0060	0.0150	48,185	0.375
1H-1	1,375	795,217	21,032	0.487	1.379	2,142,968	26.87	76.08	9,576	0.0077	0.0218	41,151	0.320
1H-1	1,400	758,584	23,438	0.543	1.241	2,650,436	33.23	75.99	10,547	0.0085	0.0194	46,610	0.363
1H-1	1,425	586,722	20,293	0.470	1.017	2,783,249	34.90	75.49	8,328	0.0067	0.0145	47,630	0.371
1H-2	25	538,343	18,325	0.424	1.453	1,571,684	19.71	67.50	8,918	0.0072	0.0245	141,444	1.101
1H-2	50	787,958	15,936	0.369	1.059	2,226,434	27.92	80.11	7,310	0.0059	0.0168	50,681	0.394
1H-2	75	805,494	12,733	0.295	1.068	1,770,030	22.19	80.39	4,380	0.0035	0.0127	80,342	0.625
1H-2	100	784,573	17,289	0.400	1.534	1,467,440	18.40	70.50	8,003	0.0064	0.0246	227,596	1.771
1H-2	125	771,104	14,781	0.342	1.410	1,343,867	16.85	69.43	5,566	0.0045	0.0184	188,299	1.465

Table T2 (continued).

Core section	Depth in section (mm)	MnO NMS	Fe area	Fe median-scale	Fe ₂ O ₃ NMS	Ba area (50kV scan)	Ba median-scaled	BaSO ₄ NMS
321-U1338A-								
1H-1	25	1.576	50,683	0.449	1.382	3,398	0.124	0.381
1H-1	50	2.090	90,042	0.797	1.865	12,199	0.444	1.040
1H-1	75	1.648	89,287	0.790	1.392	10,974	0.400	0.704
1H-1	100	1.651	90,977	0.805	1.420	9,940	0.362	0.639
1H-1	125	1.475	90,424	0.800	1.010	10,158	0.370	0.467
1H-1	150	1.129	94,039	0.832	1.033	9,623	0.350	0.435
1H-1	175	1.428	87,932	0.778	0.963	9,972	0.363	0.449
1H-1	200	1.419	89,331	0.791	1.006	9,665	0.352	0.448
1H-1	225	1.429	93,019	0.823	1.008	10,382	0.378	0.463
1H-1	250	1.100	87,689	0.776	0.971	9,772	0.356	0.445
1H-1	275	1.913	96,548	0.854	0.974	10,461	0.381	0.434
1H-1	300	1.747	92,263	0.816	0.951	10,614	0.386	0.450
1H-1	325	0.440	87,897	0.778	0.962	9,471	0.345	0.426
1H-1	350	0.369	91,854	0.813	0.955	10,186	0.371	0.436
1H-1	375	0.291	78,209	0.692	0.862	8,369	0.305	0.380
1H-1	400	0.303	79,233	0.701	0.882	8,851	0.322	0.405
1H-1	425	0.316	79,555	0.704	0.847	8,692	0.317	0.381
1H-1	450	0.317	70,631	0.625	0.815	8,189	0.298	0.389
1H-1	475	0.409	68,976	0.610	0.885	8,088	0.295	0.427
1H-1	500	0.345	75,054	0.664	0.924	8,452	0.308	0.428
1H-1	525	0.287	69,963	0.619	0.845	7,515	0.274	0.373
1H-1	550	0.185	70,260	0.622	0.759	7,402	0.270	0.329
1H-1	575	0.226	69,223	0.613	0.805	7,482	0.272	0.358
1H-1	600	0.164	62,797	0.556	0.759	5,850	0.213	0.291
1H-1	625	0.190	70,224	0.621	0.713	6,139	0.224	0.257
1H-1	650	0.175	55,641	0.492	0.652	5,944	0.216	0.286
1H-1	675	0.538	67,879	0.601	0.737	6,751	0.246	0.302
1H-1	700	0.395	67,904	0.601	0.748	6,692	0.244	0.303
1H-1	725	0.465	66,785	0.591	0.704	6,742	0.246	0.292
1H-1	750	0.391	59,237	0.524	0.755	7,112	0.259	0.373
1H-1	775	0.264	62,104	0.550	0.698	6,532	0.238	0.302
1H-1	800	0.303	67,662	0.599	0.776	6,624	0.241	0.312
1H-1	825	0.455	59,105	0.523	0.778	6,967	0.254	0.377
1H-1	850	0.631	65,050	0.576	0.810	6,810	0.248	0.349
1H-1	875	0.303	76,096	0.673	0.794	6,822	0.248	0.293
1H-1	900	0.407	62,327	0.552	0.821	6,855	0.250	0.372
1H-1	925	0.312	63,732	0.564	0.850	6,243	0.227	0.343
1H-1	950	0.251	71,860	0.636	0.921	7,165	0.261	0.378
1H-1	975	0.254	70,781	0.626	0.861	7,286	0.265	0.365
1H-1	1,000	0.242	73,703	0.652	0.775	6,210	0.226	0.269
1H-1	1,025	0.384	69,539	0.615	0.810	6,541	0.238	0.313
1H-1	1,050	0.647	67,783	0.600	0.887	6,657	0.242	0.359
1H-1	1,075	0.803	73,135	0.647	1.151	6,530	0.238	0.423
1H-1	1,100	0.657	53,512	0.474	1.036	6,996	0.255	0.557
1H-1	1,125	0.936	81,515	0.721	1.155	7,629	0.278	0.445
1H-1	1,150	0.567	72,320	0.640	1.309	6,332	0.231	0.472
1H-1	1,175	0.990	113,512	1.004	1.828	10,023	0.365	0.664
1H-1	1,200	0.533	66,715	0.590	1.186	7,926	0.289	0.580
1H-1	1,225	0.756	111,562	0.987	1.803	9,933	0.362	0.660
1H-1	1,250	0.861	127,247	1.126	3.180	13,312	0.485	1.369
1H-1	1,275	0.571	104,438	0.924	2.028	7,418	0.270	0.593
1H-1	1,300	1.179	148,491	1.314	5.033	16,535	0.602	2.306
1H-1	1,325	0.918	176,752	1.564	4.657	16,931	0.617	1.835
1H-1	1,350	0.943	179,690	1.590	4.000	14,622	0.532	1.339
1H-1	1,375	0.907	198,901	1.760	4.984	16,031	0.584	1.653
1H-1	1,400	0.829	210,526	1.863	4.260	16,623	0.605	1.384
1H-1	1,425	0.802	153,476	1.358	2.938	10,865	0.396	0.856
1H-2	25	3.770	190,726	1.688	5.781	12,023	0.438	1.500
1H-2	50	1.132	163,752	1.449	4.158	14,198	0.517	1.484
1H-2	75	2.265	155,479	1.376	4.984	14,498	0.528	1.912
1H-2	100	6.786	203,431	1.800	6.898	19,959	0.727	2.785
1H-2	125	6.037	179,374	1.587	6.541	15,976	0.582	2.397